Online supplement for "Disrupt the upper or the lower conduit? The dual role of gas exsolution in the conduits of persistently active volcanoes"

This appendix is structured into two main sections. The first section provides a verification of our numerical model, and the second section summarizes additional simulations we have performed to test the role of different non-dimensional parameters on the flow behavior.

1 Verification of our numerical approach using analytical estimates for wave speeds

Applying the general shock theory summarized in LeVeque (2002) to the model, we have two constraints for any shock, given uniform core properties. The first is the Rankine-Hugoniot condition,

$$U_s = \frac{1}{\pi}\frac{Te_u - Te_l}{\alpha_u - \alpha_l}, \tag{1}$$

where U_s is the shock velocity, $Te_u = Te(\alpha_u)$, $Te_l = Te(\alpha_l)$, $\alpha_u = \alpha(z \to z_s^+)$, and $\alpha_l = \alpha(z \to z_s^-)$, where z_s is the location of the shock. The second is the Oleinik entropy condition,

$$\frac{1}{\pi}\frac{Te - Te_l}{\alpha - \alpha_l} \geq U_s \geq \frac{1}{\pi}\frac{Te - Te_u}{\alpha - \alpha_u} \quad \text{for all } \alpha \text{ between } \alpha_l \text{ and } \alpha_u\,. \tag{2}$$

According to Dauck *et al.* (2019), the first condition comes from mass conservation across the shock, and the second condition corresponds to the internal consistency of the shock.

To verify the accuracy of our numerical method, we use the Rankine-Hugoniot condition to constrain the shock speed and a similarity solution to describe the formation and quantify the propagation speed of centered rarefaction waves explicitly (Mirzaeian & Alba, 2018). With constant core properties and using a similarity parameter, $\lambda = z/t$, we can rewrite equation (2.23) as, for $t > 0$,

$$-\frac{\lambda}{t}\frac{\mathrm{d}\bar{\alpha}}{\mathrm{d}\lambda} + \frac{1}{t}\frac{\partial Te}{\partial \bar{\alpha}}\frac{\mathrm{d}\bar{\alpha}}{\mathrm{d}\lambda} = 0 \quad \text{with} \quad \bar{\alpha}(\lambda) = \alpha(z,t). \tag{3}$$

We find that either $\mathrm{d}\bar{\alpha}/\mathrm{d}\lambda = 0$, which gives a trivial solution $\bar{\alpha} = \text{constant}$, or

$$\lambda = \frac{\partial}{\partial \bar{\alpha}} Te(\bar{\alpha}, \varphi, \psi). \tag{4}$$

Rarefactions form where the upstream kinematic wave speed is slower than the upstream speed, i.e. $\partial Te/\partial\alpha$ and $\partial^2 Te/\partial\alpha\partial z$ have the same sign, yielding the constraint

$$(\partial Te/\partial\alpha)(\partial^2 Te/\partial\alpha\partial z) > 0\,. \tag{5}$$

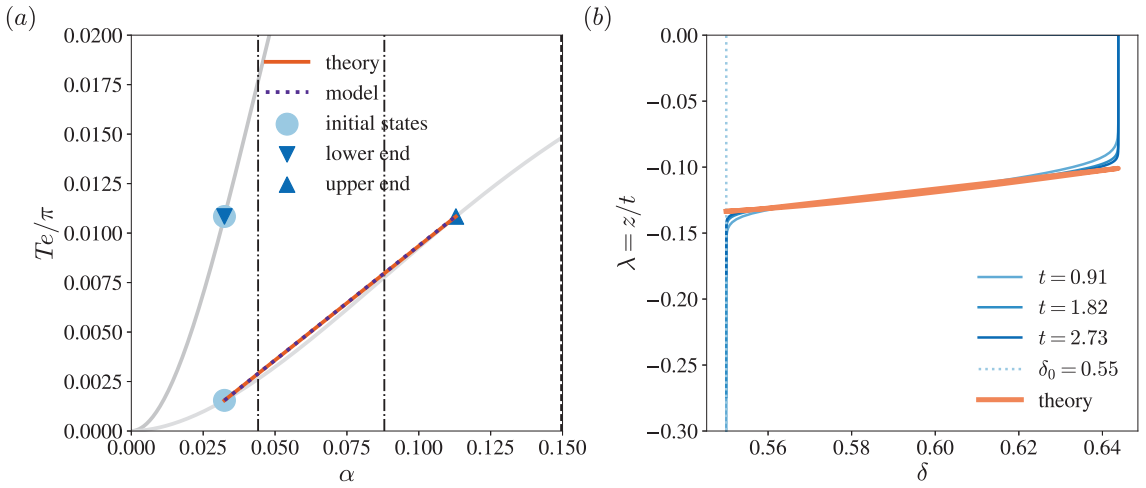

Figure S1: Shock and rarefaction comparisons between theory and simulation. Panel (a) is a zoom-in of figure 9 (a) and shows the speed for an ascending shock in the Te/π-α space. And panel (b) is a zoom-in of figure 9 (h) with a transformed y-axis and shows the similarity solution for a descending rarefaction.

It describes regions where the kinematic wave speed increases consistently along the wave propagation direction. With both φ and ψ being constant, we have $\alpha(z,t) = \bar{\alpha}(\lambda) = (\partial Te/\partial\alpha)^{-1}(\lambda)$ representing the propagation of a rarefaction fan.

We compare these analytical results for propagation speeds of both shocks and rarefactions with simulation results and find consistency. Figure S1 (a) shows a zoom-in of figure 9 (a). In the Te-α diagram, solid orange line gives the shock speed based on Rankine-Hugoniot condition, while dotted purple is the estimated shock speed from simulation. We obtain the estimate by picking the shock front at two time steps, calculating the distance, and dividing it by the time difference. The collapse of the two lines indicates that our numerical model agrees well with theory. Figure S1 (b) illustrate similarity solutions of rarefactions from both theory and model. It corresponds to figure 9 (h) except for the zoom-in view and a transformed y axis. Solutions of $\delta(z,t)$ at different t collapse onto each other when we use the similarity parameter $\lambda = z/t$ as the y axis. They also coincide with the solution predicted by theory. We conclude that our numerical model captures the propagation behavior of shock and rarefaction waves.

2 Additional simulation results

2.1 Complete results for step changes in core density

We provide complete simulation results for a 5% drop in core density at $z = 0$ in figures S2 and S3. To map out the full set of different dynamic regimes arising from the nonconvexity of the flux function, we choose seven different initial conditions of core radius

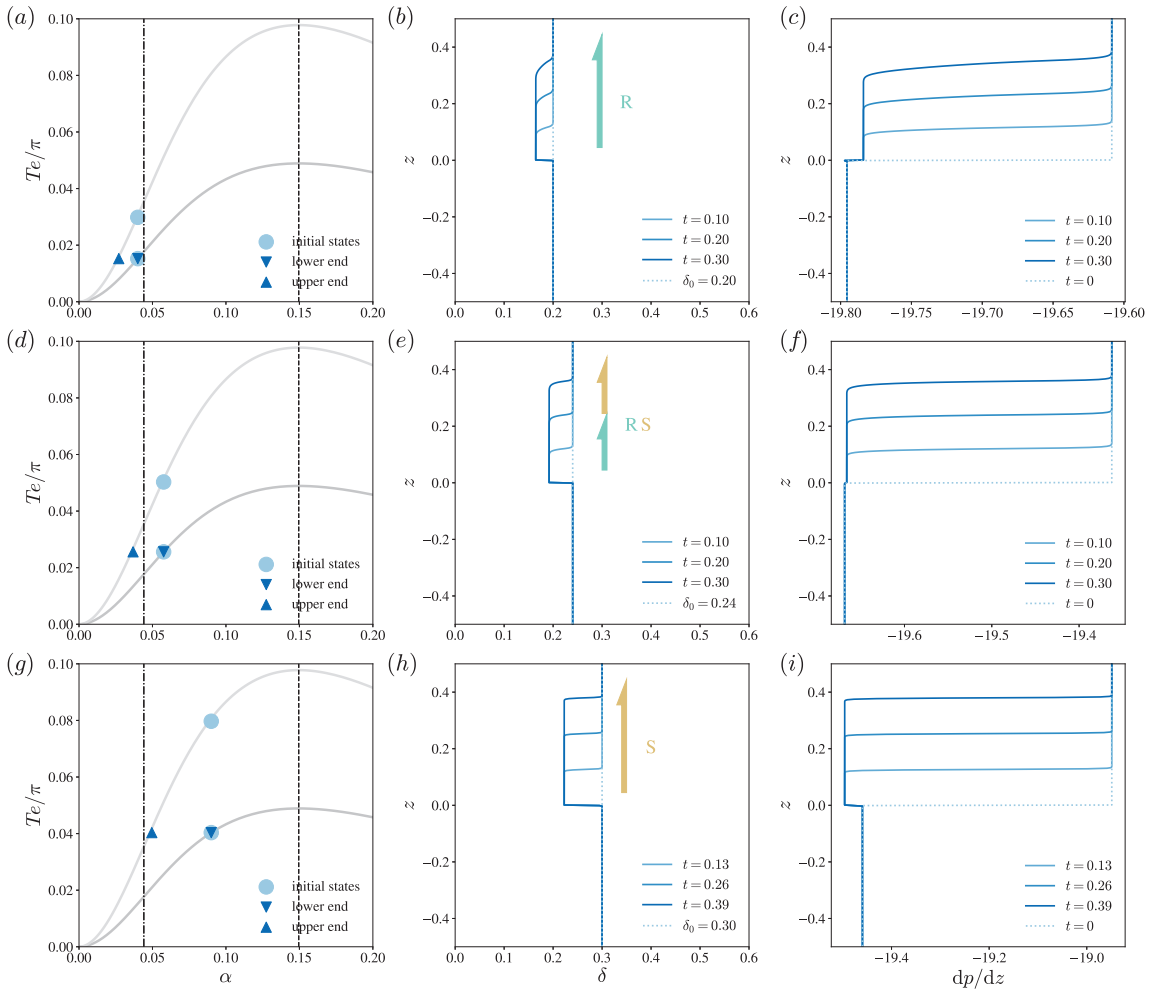

Figure S2: Simulation results for a 5% drop in core density at $z = 0$ and various uniform initial core thicknesses δ_0, representing first three dynamic regimes in figure 10 (a). The left, middle and right columns represent Te-α diagrams, core thickness evolution, and total pressure gradient change, similarly to figure 8. In all simulations, $\mathcal{R} = 0.95$, $M = 100$, $\Delta_\mu = 0$ and $\Delta_\rho = -1/19$.

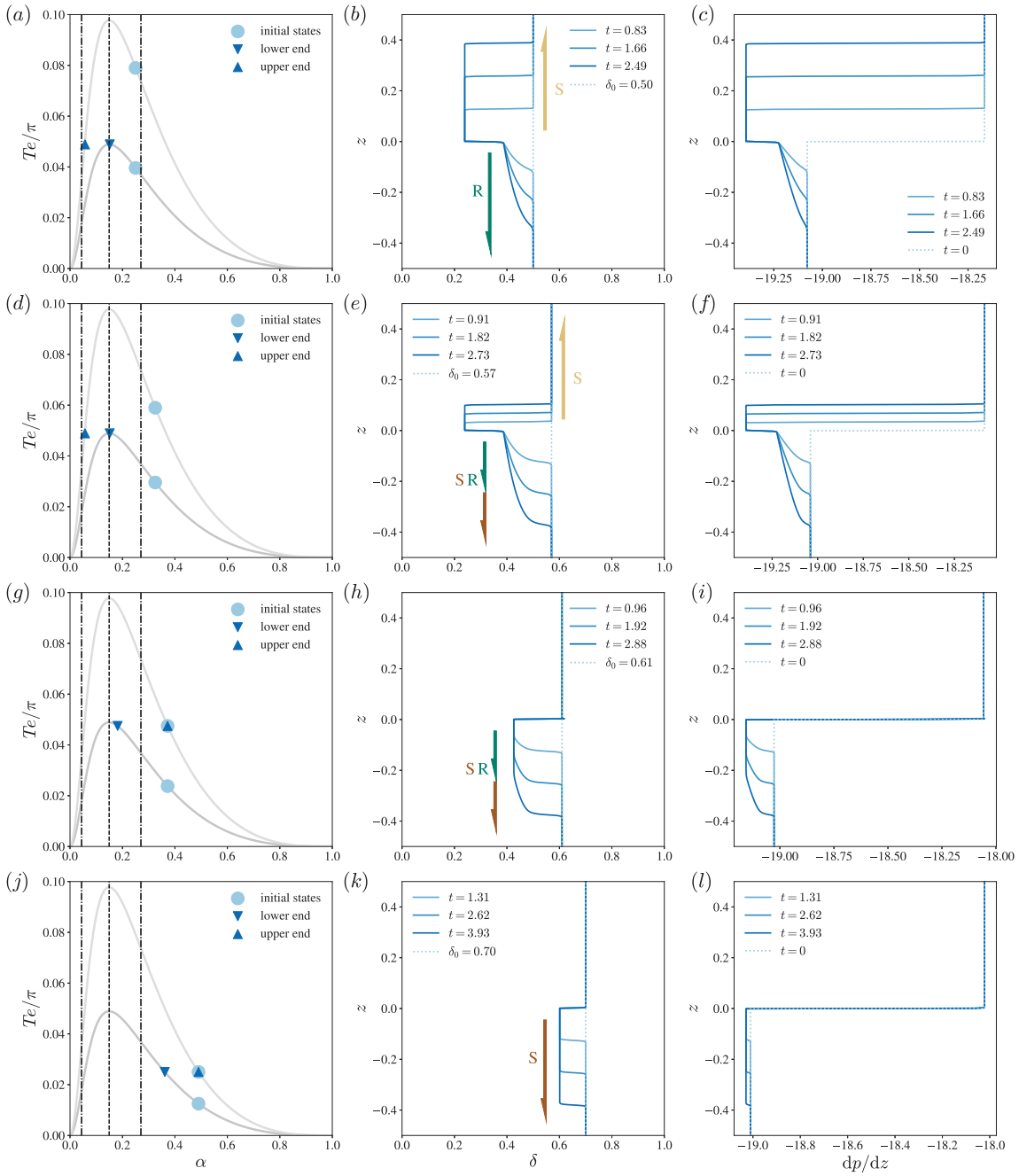

Figure S3: Simulation results for a 5% drop in core density at $z = 0$ and various uniform initial core thicknesses δ_0, representing last four dynamic regimes in figure 10 (a). The left, middle and right columns represent Te-α diagrams, core thickness evolution, and total pressure gradient change, similarly to figure 8. In all simulations, $\mathcal{R} = 0.95$, $M = 100$, $\Delta_\mu = 0$ and $\Delta_\rho = -1/19$.

$\delta_0 = 0.20, 0.24, 0.30, 0.50, 0.57, 0.61, 0.70$. Each row corresponds to a refined dynamic regime in figure 10 (a).

As volatile exsolution decreases the core density, the driving force increases in the upper portion of the domain, leading to elevated flux in the upper domain (light grey curve) as compared to the lower domain (dark grey curve) in figure S2(a,d,g) and figure S3(a,d,g,j). The light blue dots on these curves represent the initial, somewhat hypothetical state of the two domains. The flux deficit between the two initial states drives rapid adjustment of the core radius at $z = 0$, resulting in the formation of a stationary shock that balances the fluxes in the two domains. The final fluxes are shown as dark blue triangles, with triangle representing the lower conduit pointing down and the one representing the upper conduit pointing up.

Where within the volcanic conduit the flow adjustment takes place depends on the core thickness or, equivalently, the core volume fraction. To highlight this dependence, we show the flooding volume fraction $\alpha_{FP} = \delta_{FP}^2$ as a dashed line in figures S2 and S3, and the inflection volume fractions as dash-dotted lines. For the small volume fractions shown in figure S2, only the upper portion of the conduit adjusts, as illustrated by the light blue dot and downward pointing triangle coinciding. In the broad vicinity of the flooding point, the flow field in the entire conduit is adjusting, as is the case in figures S3(a,d). At sufficiently large core thickness, only the lower conduit responds to gas exsolution as shown in figures S3(g,j).

Our simulations illustrate three basic types of waves and four compound wave fields. In the middle columns of figures S2 and S3, we show snapshots of the core radius $\delta(z,t)$ with consistent colored arrows and letters indicating types and propagation directions of waves. The light blue dotted lines show the initially uniform core radius, δ_0, and the solid curves with increasingly dark shades of blue show the evolution as time progresses. Figures S2 shows the case when the initial core thicknesses are well below the flooding point. In the limit $\delta_0 < \delta_{I1}$, only an ascending rarefaction forms (b). A slightly larger initial core thickness is associated with an upward propagating compound wave consisting of both a shock and a rarefaction (e). The rarefaction component disappears when the first inflection point is exceeded, $\delta_0 > \delta_{I1}$, yielding a pure shock (h). This ascending shock persists as long as the initial flux of the upper domain is greater than the flooding point flux of the lower domain, but its velocity decreases as δ_0 increases.

If the initial core thickness becomes comparable to the flooding point in figure S3, an additional constraint arises. The overall flux in the entire conduit can not exceed the flux at either of the two flooding points, at least not within the confines of buoyancy-driven core-annular flow, and the overall flux becomes limited by the flooding flux in the lower conduit. As a consequence, both portions of the conduit are forced to adjust: The flux-balanced core radius in the upper domain must adjust to the flux at the flooding point in the lower domain and the flux-balanced core radius of the lower domain must be at the flooding point. The resulting compound wave field is particularly complex and consists of an ascending shock and a descending wave that is either a pure rarefaction (b) or consists of both a rarefaction and a shock (e). The ascending branch of the wave field, however, disappears once the initial flux of the upper domain becomes less than the flooding point

flux of the lower domain as is the case in (h) and (k).

2.2 Complete results for step changes in core viscosity

We also show a comprehensive summery of model results for a nine-fold increase in core viscosity at $z = 0$ in figures S4 and S5. They exhibit total 7 refined regimes in figure 10 (c).

Similarly to the density jump controlling behavior in the previous section, it is now the viscosity ratio and jump that defines the shapes and difference between the flux functions in the lower and upper domains and the resulting wave dynamics. Figures S4 and S5 display our simulation results for the case of a finite jump in core viscosity. We assume an initial viscosity contrast between core and annulus magma of $M = 100$, neglect the density jump entirely, $\Delta_\rho = 0$, and instead impose a sudden increase in the core viscosity by almost an order of magnitude $\Delta_\mu = 9$. The constant density contrast between core and annulus magma is $\mathcal{R} = 0.95$ and we consider the initial core thickness of $\delta_0 = 0.18, 0.20, 0.25, 0.35, 0.45, 0.52, 0.55$.

When the core viscosity increases, as would typically be the case as a consequence of crystallization, the flux curve for the lower domain (dark grey) is higher than for the upper domain (light grey). Since the viscosity jump shifts the positions of flooding and inflection points (see §3.1), the three critical radii for the wave dynamics come from different flux curves. In the Te/π-α diagrams, figure S4(a,d,g), the left dash-dotted line and the dashed line correspond to squares of the left inflection and flooding points of the lower flux curve, respectively. The right dash-dotted line is the square of the right inflection point of the higher flux curve. These critical points determine the evolution of dynamic waves in the second and third columns in a similar way as in the case of a jump in core density.

If the initial core thickness, δ_0, is smaller than the left inflection point and the initial flux of the lower domain is less or equal to the flooding point flux of the upper domain, only an ascending shock or compound wave form as in the case of figure S4(b,e). If δ_0 increases such that the initial flux of the lower domain is greater than the flooding point flux of the upper domain, a descending shock forms along with an ascending compound wave, e.g., figure S4(h). When δ_0 is larger than the left inflection point, the ascending wave becomes a pure rarefaction as demonstrated in figure S5(b). As δ_0 increases further, the descending wave transforms into a compound wave and finally a pure rarefaction in the case of figure S5(b,e,h,k). The ascending branch, however, disappears once δ_0 increases beyond the flooding point.

2.3 Smooth profiles of core properties suggest consistent behavior

The goal of this paper is to understand how core-annular flow responds to a sudden change in the density and viscosity of the core magma as a consequence of bubble nucleation. We model the implications of bubble nucleation as a discontinuous change in core density and viscosity when, in reality, the change would be continuous at small spatial scales. To assess that our results are robust to steep but smooth transition, we performed simulations with

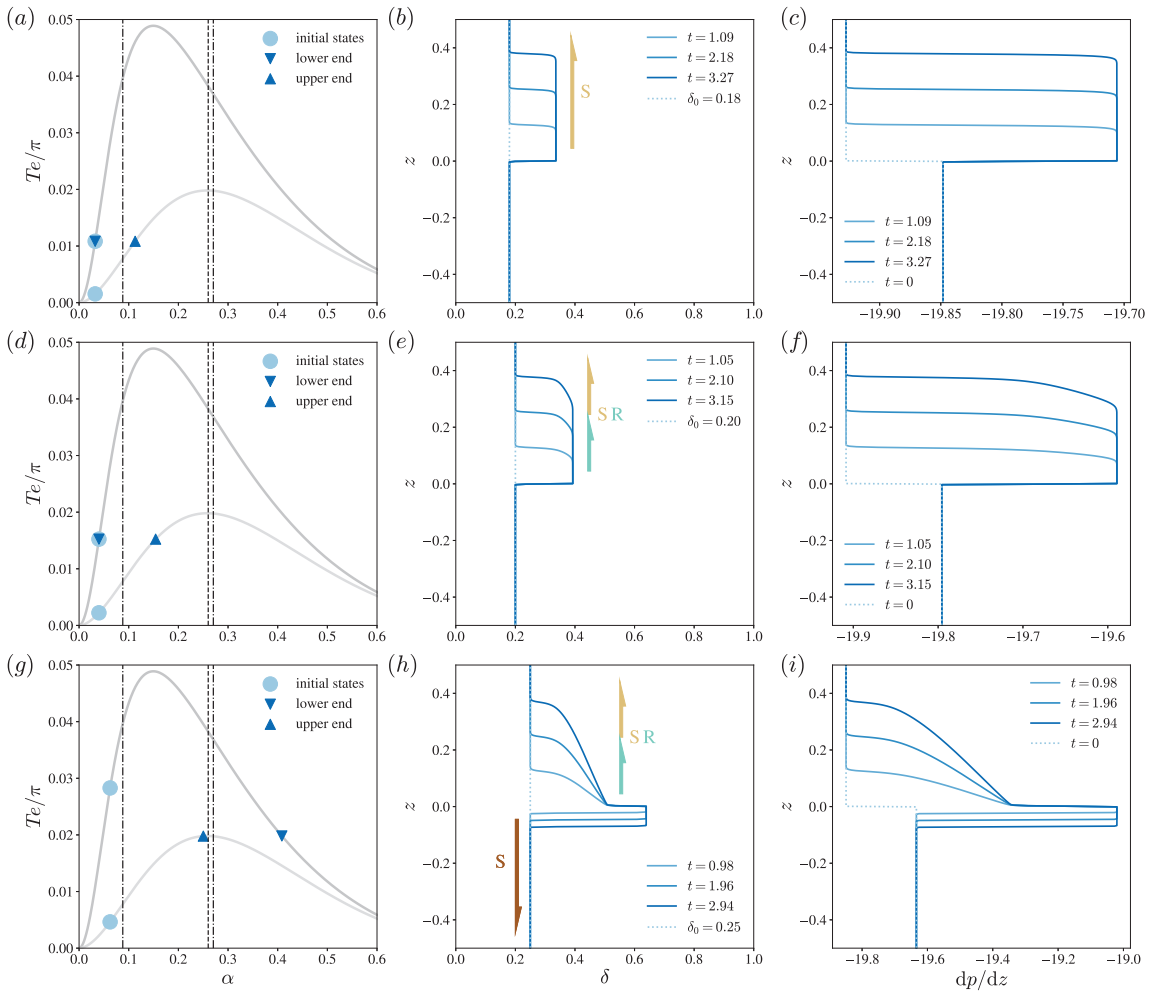

Figure S4: Simulation results for a nine-fold increase in core viscosity at $z = 0$ and various uniform initial core thicknesses δ_0. The left, middle and right columns represent Te-α diagrams, core thickness evolution, and total pressure gradient change, similarly to figure 9. In all simulations, $\mathcal{R} = 0.95$, $M = 100$, $\Delta_\mu = 9$, and $\Delta_\rho = 0$.

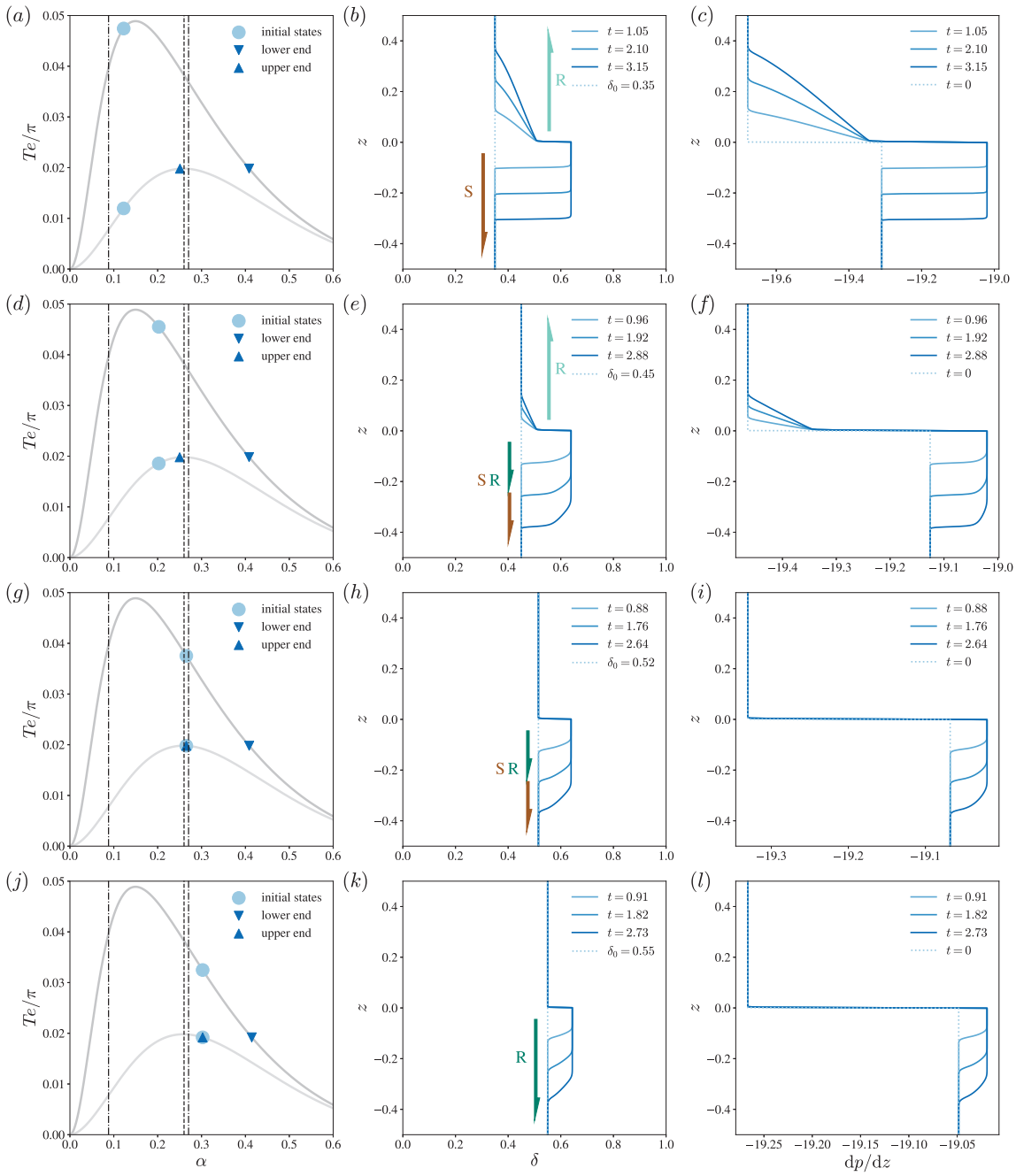

Figure S5: Simulation results for a nine-fold increase in core viscosity at $z = 0$ and various uniform initial core thicknesses δ_0. The left, middle and right columns represent Te-α diagrams, core thickness evolution, and total pressure gradient change, similarly to figure 9. In all simulations, $\mathcal{R} = 0.95$, $M = 100$, $\Delta_\mu = 9$, and $\Delta_\rho = 0$.

smooth profiles of core properties.

In particular, we generalize equations (2.3) and (2.4) to

$$\rho_c(z) = \rho_0(1+\Delta_\rho f_\rho(z)), \tag{6}$$
$$\mu_c(z) = \mu_0(1+\Delta_\mu f_\mu(z)), \tag{7}$$

where $f_\rho(z)$ and $f_\mu(z)$ are smooth functions in z. We assume that $|f_\rho(z)| \le 1$ and that $|f_\mu(z)| \le 1$. The same derivation gives again equation (2.15), with

$$\varphi(z) = \frac{M}{1+\Delta_\mu f_\mu(z)}, \quad \psi(z) = 1 - \frac{\mathcal{R}\Delta_\rho f_\rho(z)}{1-\mathcal{R}}. \tag{8}$$

The generalized exchange-flow condition (2.17), in integrated form, becomes

$$\frac{\Delta_\rho f_\rho'(z)}{1+\Delta_\rho f_\rho(z)} \int_0^\delta r u_c \mathrm{d}r + \frac{\partial}{\partial z}\left(\int_0^\delta r u_c \mathrm{d}r + \int_\delta^1 r u_a \mathrm{d}r\right) = 0. \tag{9}$$

Explicitly, we have

$$\int_0^\delta r u_c \mathrm{d}r = -\delta^2 \frac{P\left[2-\delta^2(2-\varphi)\right] - \delta^2\psi(\varphi - 4\ln\delta)}{16}, \tag{10}$$
$$\int_0^\delta r u_c \mathrm{d}r + \int_\delta^1 r u_a \mathrm{d}r = -\frac{P\left[1-\delta^4(1-\varphi)\right] - \delta^2\psi\left[2-\delta^2(2-\varphi)\right]}{16}. \tag{11}$$

The same conservation law applies

$$\frac{\partial \delta^2}{\partial t} + \frac{\partial}{\partial z}\left(\frac{Te}{\pi}\right) = \frac{\partial \delta^2}{\partial t} - 2\frac{\partial}{\partial z}\left(\int_\delta^1 r u_a \mathrm{d}r\right) = 0, \tag{12}$$

where

$$\int_\delta^1 r u_a \mathrm{d}r = -\frac{\left(1-\delta^2\right)\left[P\left(1-\delta^2\right) - 2\delta^2\psi\right] - 4\delta^4\psi\ln\delta}{16}. \tag{13}$$

Together with (9), this equation forms a system that solves for $P(z,t)$ and $\delta(z,t)$, given φ and ψ. But equation (9) is not in a conserved form, which implies that we cannot apply our numerical method directly. Therefore, we use asymptotic analysis to simplify the system based on real magma property variations and numerical results with step-like core density changes.

During phases of passive degassing, core density can realistically change only by a few percent. Our numerical results with step changes indicate that correction terms in (2.20) and (2.21) due to Δ_ρ have minor effect in our conclusions. Therefore, we seek an asymptotic expansion in P in terms of small Δ_ρ

$$P = P^{(0)} + \Delta_\rho P^{(1)} \ldots. \tag{14}$$

Substituting into (2.4) and letting $\Delta_\rho \to 0$ yields

$$\frac{\partial}{\partial z}\left\{P^{(0)}\left[1-\delta^4(1-\varphi)\right] - \delta^2\left[2-\delta^2(2-\varphi)\right]\right\} = 0. \tag{15}$$

With the same no net flux boundary condition at $z_0 = -0.5$, we have

$$P^{(0)} = \delta^2 \frac{2 - \delta^2 (2 - \varphi)}{1 - \delta^4 (1 - \varphi)}. \tag{16}$$

This coincides with the full driving force P when $\Delta_\rho = 0$. Similarly, for $\mathrm{O}(\Delta_\rho)$ we have

$$\frac{\partial}{\partial z} \left\{ P^{(1)} \left[1 - \delta^4 (1 - \varphi) \right] + \frac{\mathcal{R} f_\rho}{1 - \mathcal{R}} \delta^2 \left[2 - \delta^2 (2 - \varphi) \right] \right\} = \\ f'_\rho \left\{ P^{(0)} \left[2 - \delta^2 (2 - \varphi) \right] - \delta^2 (\varphi - 4 \ln \delta) \right\}. \tag{17}$$

Thus,

$$P^{(1)} = -\frac{\mathcal{R} f_\rho}{1 - \mathcal{R}} \delta^2 \frac{2 - \delta^2 (2 - \varphi)}{1 - \delta^4 (1 - \varphi)} + I, \tag{18}$$

where the integral

$$I = \int_{z_0}^{z} f'_\rho \delta^2 \left\{ \frac{\left[2 - \delta^2 (2 - \varphi) \right]^2}{1 - \delta^4 (1 - \varphi)} - \varphi + 4 \ln \delta \right\} \mathrm{d}z. \tag{19}$$

The two terms in $P^{(1)}$ consist of contributions from the magnitude f_ρ and gradient f'_ρ of core density variation, respectively. We use trapezoidal rule to calculate this integral at each time step to update P for our numerical method.

Results with smooth variations in either core density or viscosity are consistent with our Riemann problem. Figure S6 is equivalent to the right two columns in figure 8, with same Δ_ρ yet $f_\rho = (1 + \tanh z/l_\rho)/2$ and $l_\rho = 0.05$. We observe similar wave propagation patterns away from $z = 0$ but what appeared as a stationary shock at the nucleation depth is now a smooth transition in core thickness. The distinction between shocks and rarefactions in the wave field is clearer in the smooth case. We also note that the pressure gradient for $z > 0$ varies with time in a uniform fashion, which is not the case in the Riemann problem. Results with smooth viscosity variations also show general consistencies compared with their Riemann counterparts. Figure S7 is equivalent to the last two columns in figure 9, with same Δ_μ yet $f_\mu = (1 + \tanh z/l_\mu)/2$ and $l_\mu = 0.05$. Apart from the smooth variation around $z = 0$, the propagation of perturbation agrees well between the two.

2.4 Parameter test with various Δ_ρ and Δ_μ

In principle, we can apply our techniques to explore the parameter space of core property changes and study how propagation of information varies. Here, we show a few examples of these exploration, but note that a comprehensive search in the parameter space is not the focus of this work. The density jump, Δ_ρ, simply determines the magnitude difference of two flux functions, and can change some dynamic regime boundaries that do not overlap with three critical radii (see figure S8(a,b)). The viscosity jump, Δ_μ, shift these critical points and has greater flexibility in changing the regime pattern (see figure S8(c,d)). The

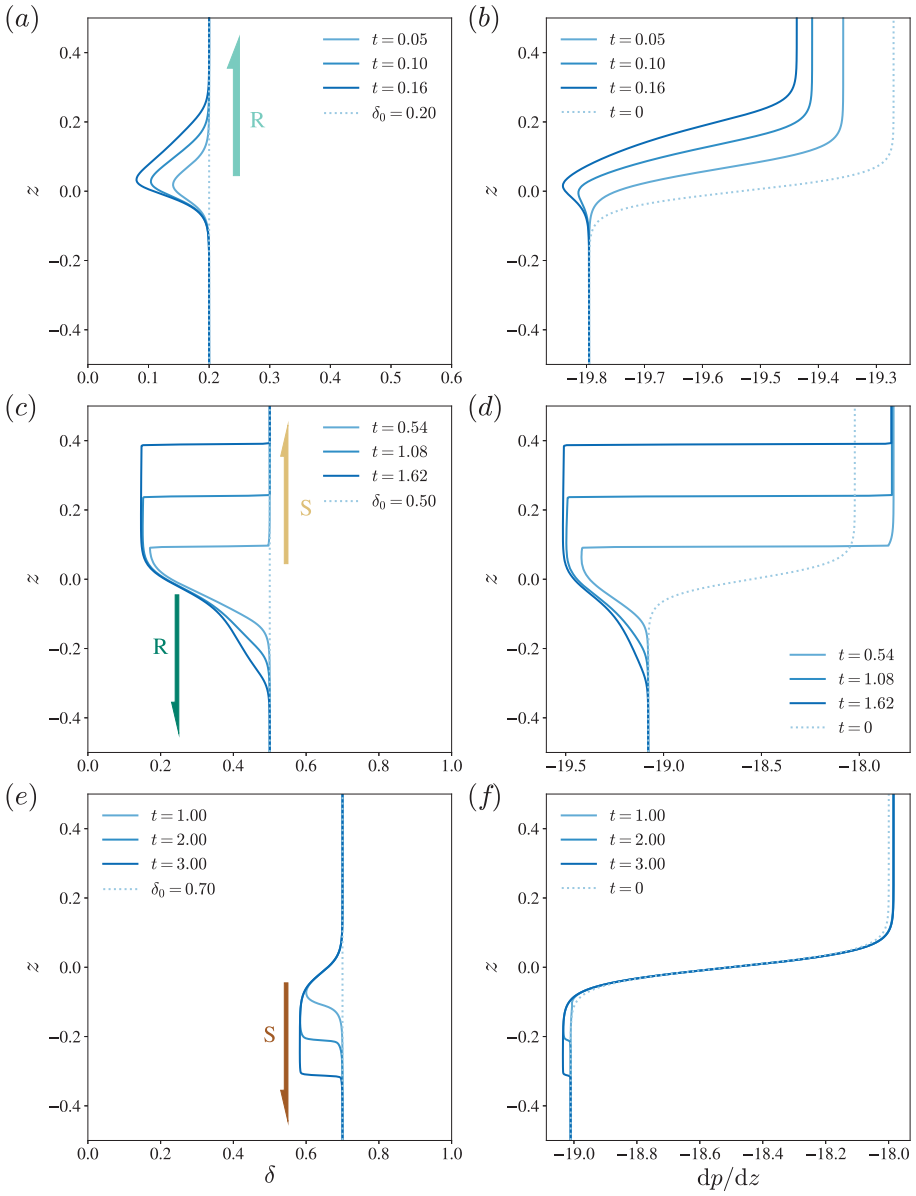

Figure S6: Simulation results with a smooth core density variation around $z = 0$ and various uniform initial core radii δ_0. The left, and right columns represent core radius evolution, and total pressure gradient change. In all simulations, $\mathcal{R} = 0.95$, $M = 100$, $\rho_c(z)/\rho_0 = 1 - (1 + \tanh z/l_\rho)/38$, $l_\rho = 0.05$, and $\mu_c(z)/\mu_0 = 1$, representing an smooth decrease in core density. The choice of initial core radii is identical to that in figure 8.

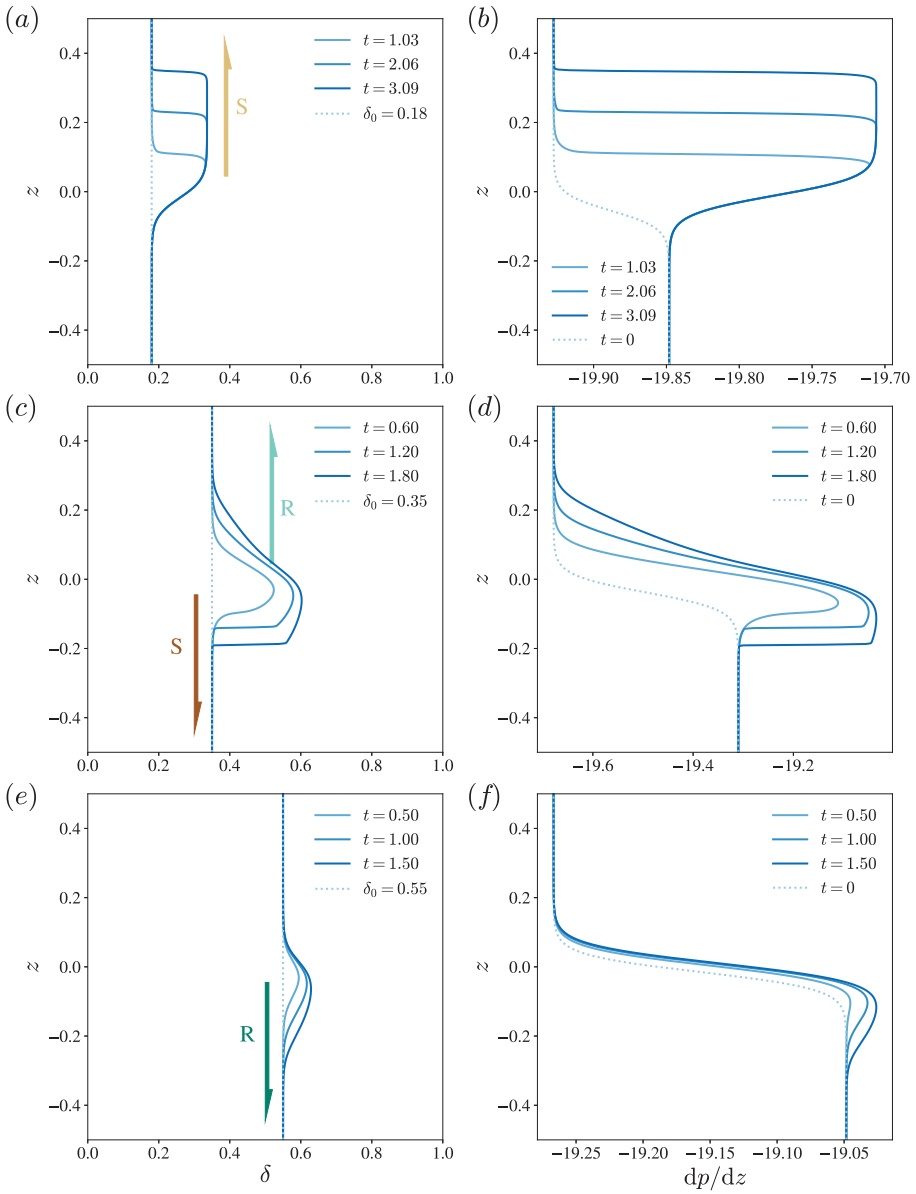

Figure S7: Simulation results with a smooth core viscosity variation around $z = 0$ and various uniform initial core radius δ_0. The left, and right columns represent core radius evolution, and total pressure gradient change. In all simulations, $\mathcal{R} = 0.95$, $M = 100$, $\mu_c(z)/\mu_0 = 1 + 9(1 + \tanh z/l_\mu)/2$, $l_\mu = 0.05$, and $\rho_c(z)/\rho_0 = 1$, representing an smooth increase in core viscosity. The choice of initial core radii is identical to that in figure 9.

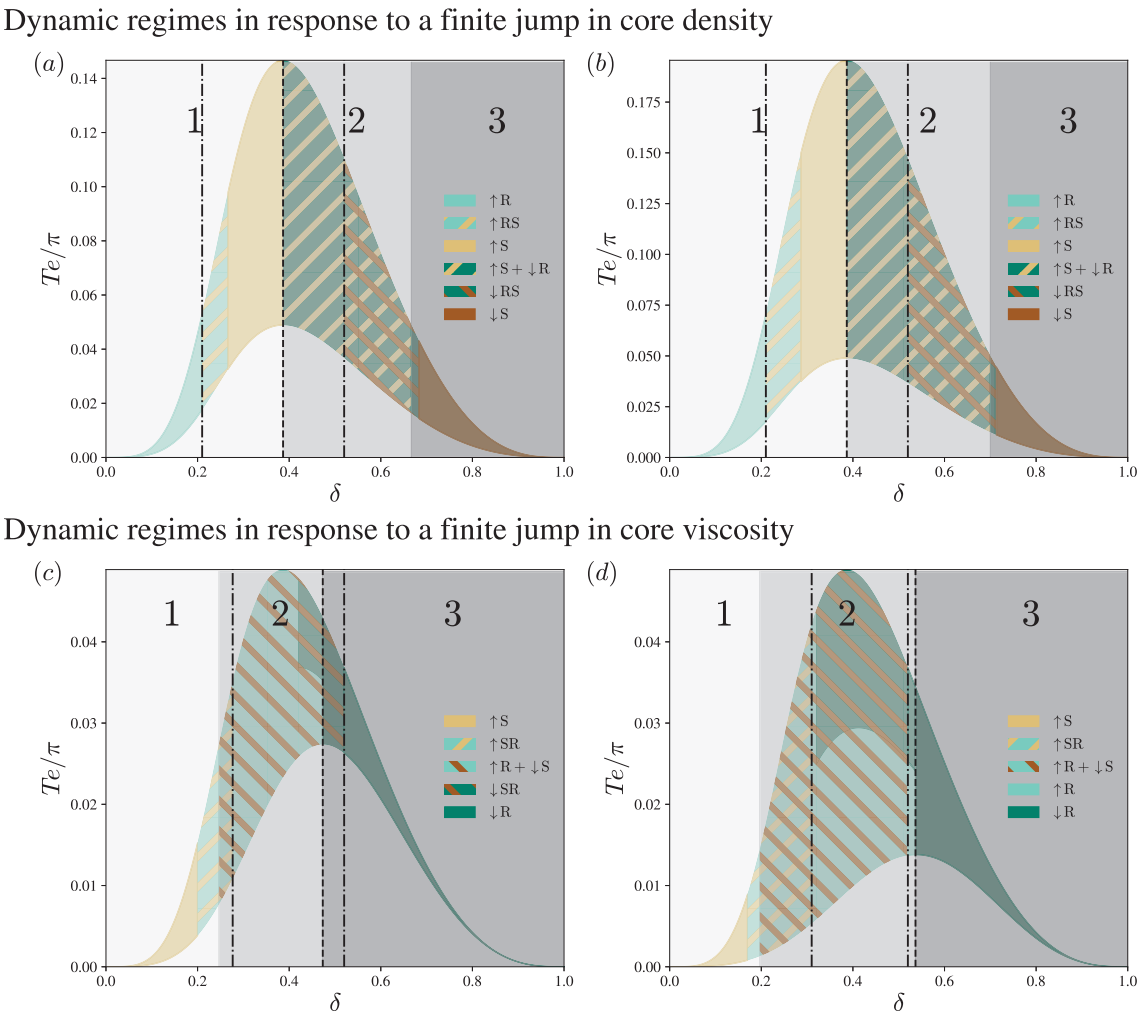

Figure S8: Wave field categorizations with constant initial core radius δ_0. In all cases, $\mathcal{R} = 0.95$, and $M = 100$. Panels (a)-(b) represent cases with $\Delta_\mu = 0$, $\Delta_\rho = -2/19$ and $\Delta_\rho = -3/19$, respectively. Panels (c)-(d) represent cases with $\Delta_\rho = 0$, $\Delta_\mu = 4$ and $\Delta_\mu = 19$, respectively. The dashed line and the dash-dotted line on the left indicate the flooding and left inflection points of the lower flux function, while the dash-dotted line on the right represents the right inflection point of the higher flux function.

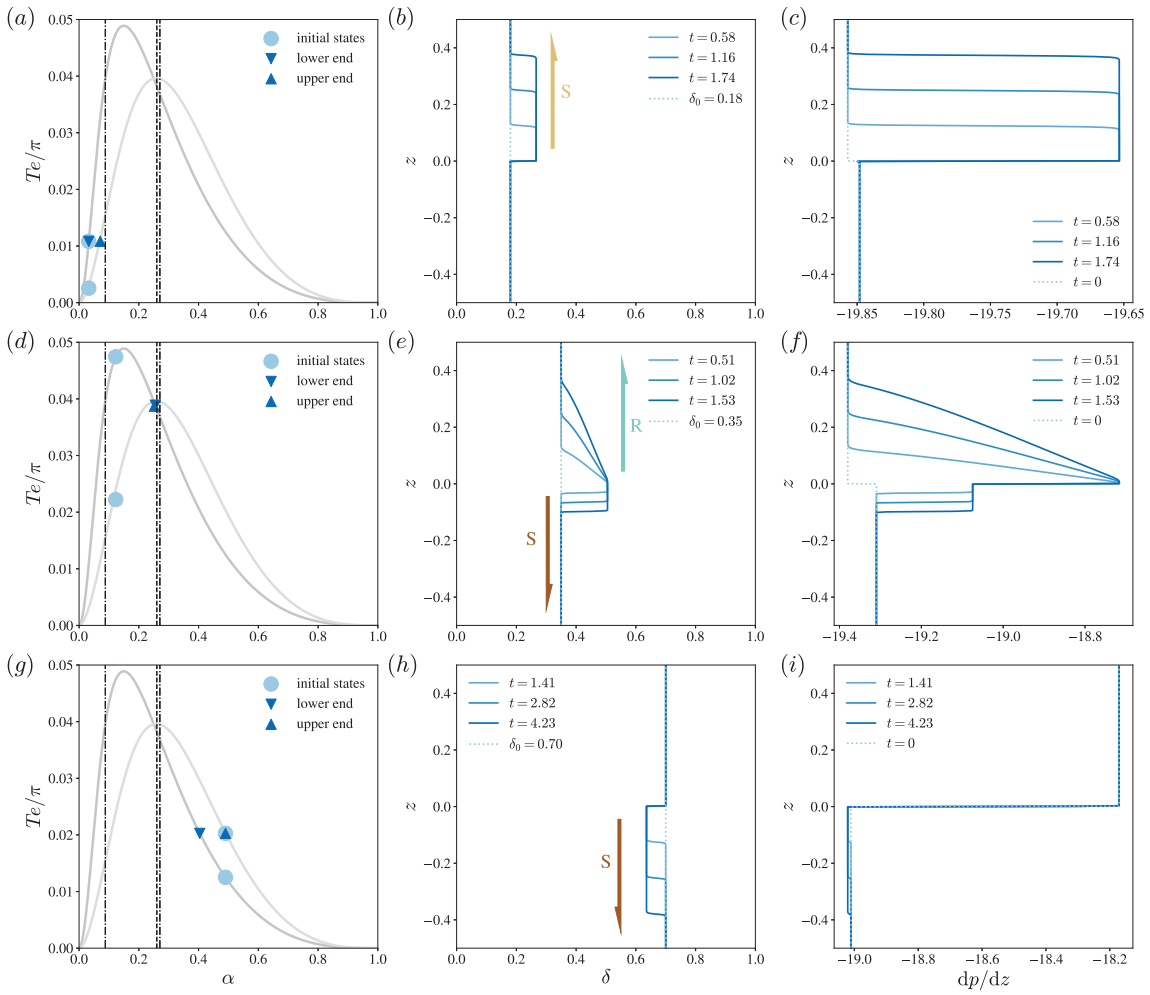

Figure S9: Simulation results for a change in both core density and viscosity jumps at $z = 0$, initiated by various uniform initial core radii, δ_0. The left, and right columns represent core radius evolution, and total pressure gradient change. In all simulations, $\mathcal{R} = 0.95$, $M = 100$, $\Delta_\rho = -1/19$, $\Delta_\mu = 9$.

shift of regime boundaries is more significant with increasing core viscosity jump. Moreover, if we include both density and viscosity jumps, the two effects compete as discussed in more detail in the main manuscript. Our results indicate that viscosity jump tends to affect thin-core flow more (see and compare first two rows of figures S9 and 9) while density jump matters more in thick-core flow (see last rows of figures S9 and 8).

References

Dauck, T.-F., Box, F., Gell, L., Neufeld, J. A. & Lister, J. R. 2019 Shock formation in two-layer equal-density viscous gravity currents. *J. Fluid Mech.* **863**, 730–756.

LeVeque, R. J. 2002 *Finite Volume Methods for Hyperbolic Problems*. Cambridge University Press.

Mirzaeian, N & Alba, K 2018 Monodisperse particle-laden exchange flows in a vertical duct. *J. Fluid Mech.* **847**, 134–160.